Capillary-gravity solitary waves on water of finite depth interacting with a linear shear current

By T. Gao[1] *, P. A. Milewski*[2] *and Z. Wang*[3,4,5,†]

The problem of two-dimensional capillary-gravity waves on an inviscid fluid of finite depth interacting with a linear shear current is considered. The shear current breaks the symmetry of the irrotational problem and supports simultaneously counter-propagating waves of different types: KdV-type long solitary waves and wave-packet solitary waves whose envelopes are associated with the nonlinear Schrödinger equation. A simple intuition for the broken symmetry is that the current modifies the Bond number differently for left- and right-propagating waves. Weakly nonlinear theories are developed in general and for two particular resonant cases: the case of second harmonic resonance and long-wave/short-wave interaction. Travelling-wave solutions and their dynamics in the full Euler equations are computed numerically using a time-dependent conformal mapping technique, and compared to some weakly nonlinear solutions. Additional attention is paid to branches of elevation generalized solitary waves of KdV type: although true embedded solitary waves are not detected on these branches, it is found that periodic wave-trains on their tails can be arbitrarily small as the vorticity increases. Excitation of waves by moving pressure distributions and modulational instabilities of the periodic waves in the resonant cases described above are also examined by the fully nonlinear computations.

[1]School of Computing and Mathematical Sciences, University of Greenwich, London SE10 9LS, UK.
[2]Department of Mathematical Sciences, University of Bath, BA2 7AY, UK.
[3]Institute of Mechanics, Chinese Academy of Sciences, Beijing 100190, China.
[4]School of Engineering Science, University of Chinese Academy of Sciences, Beijing 100049, China.
[5]School of Future Technology, University of Chinese Academy of Sciences, Beijing 100049, China.
[†]Correspondence Author: Zhan Wang, Institute of Mechanics, Chinese Academy of Sciences, Beijing 100190, China. Email: zwang@imech.ac.cn

DOI: 10.1111/((please add article doi))

STUDIES IN APPLIED MATHEMATICS AA:1–28

Keywords: solitary wave, gravity-capillary wave, water wave

1. Introduction

There have been numerous investigations on free-surface water waves in the presence of both gravity and surface tension, the so-called capillary-gravity waves. Despite of a short wavelength (typically about a centimeter), these waves are believed to play an important role in transferring mass, momentum, and energy across the ocean surface [1]. For a review of basic concepts of capillary-gravity waves, the readers are referred to the monograph [2].

The motion of an inviscid, incompressible and irrotational flow with a free surface is governed by the full Euler equations which can be reduced to simplified models in various limits. Two widely used models are

$$\zeta_t + c_0\zeta_x + \frac{3c_0}{2h}\zeta\zeta_x + (1-3\mathcal{B})\frac{c_0h^2}{6}\zeta_{xxx} = 0\,, \tag{1}$$

the Korteweg de-Vries (KdV) equation valid in the shallow-water regime [3], where ζ is the surface displacement, h the mean depth of the fluid, $c_0 = \sqrt{gh}$ the long wave speed with g being the acceleration due to gravity, and $\mathcal{B} = \sigma/\rho gh^2$ the Bond number defined as the ratio of surface tension force to gravitational force with σ being the coefficient of surface tension and ρ being the fluid density, and

$$\mathrm{i}\,A_t + \lambda A_{xx} + \gamma|A|^2A = 0\,, \tag{2}$$

the nonlinear Schrödinger (NLS) equation for water of arbitrary depth, where A stands for the envelope of a monochromatic wavetrain [4], and the parameters λ and γ depend on the problem being studied. In the long-wave limit, the KdV equation (1) admits depression solitons for $\mathcal{B} > 1/3$ and elevation for $\mathcal{B} < 1/3$. The coefficients of (2) were first derived in [5] for the irrotational case and in [6] in the presence of a constant vorticity. It is well known that when $\lambda\gamma > 0$ the NLS is of focussing type and allows small-amplitude wavepackets (see [7] for example).

The existence of capillary-gravity solitary waves with damped oscillations in the full Euler equations was proved rigorously by [8, 9] in the case of finite and infinite depth, respectively. From an asymptotic point of view, the bifurcation mechanism is that the underlying NLS is of focussing type at the phase speed minimum where the group velocity equals the phase velocity [10]. Computations of such waves on deep water in the fully nonlinear equations were achieved by a boundary integral equation method in [11]. Two basic branches bifurcating from infinitesimal periodic waves were found: depression waves with a negative displacement

at their center and elevation waves with a positive displacement at their center. There are many other branches of solitary waves, e.g. asymmetric solitary waves, which can exist only at finite amplitude (see [12, 13] for more details). The dynamics and stability were studied in [14, 15] where a time-dependent conformal mapping method pioneered by [16] was employed. Depression waves are found to be stable, while the stability exchange occurs twice along the bifurcation curve of the elevation branch. In the case of finite depth, bifurcations of solitary waves depend on the value of the Bond number. If $\mathcal{B} > 1/3$, there are only depression waves bifurcating from infinitesimal long waves but no wavepacket solitary waves associated with the NLS equation (see [17]). If $\mathcal{B} < 1/3$, there exit both wavepackets and generalised solitary waves featuring an elevation hump and a non-decaying train of ripples extending up to infinity. It is emphasized that these generalised solitary waves are shown not to approach any embedded soliton solutions as a limit (i.e. along the bifurcation curve no solutions vanish completely in the far field) [18].

Meanwhile, it was derived in [4] that the modulational instability criterion simply depends on the type of the underlying NLS equation. A periodic wavetrain is modulationally stable if the NLS is of defocussing type. However, such model equation is not applicable in the case of the second harmonic resonance and long-wave/short-wave interaction since the coefficient of the nonlinear term from (2) becomes singular under these two scenarios (e.g. see [6]). Modified multi-scale analyses were achieved by [19, 20] for the former resonance and [5] for the latter one for irrotational flows. In this work, weakly nonlinear theories will be developed for the resonant cases in the presence of a linear shear current.

Ocean waves are usually accompanied by mean flows or shear currents generated by tides or winds. In reality, the initial generation and growth of capillary-gravity waves by wind are vastly influenced by the wind-induced shear current beneath the free surface [21]. As the first step towards the understanding of wave-current interactions, we restrict ourselves to the linear shear profile (i.e. constant vorticity) and to the two-dimensional problem. In this situation, solitary waves were computed in the full Euler equations using a boundary integral equation method by [22]. The NLS equation describing the envelope dynamics of a quasi-monochromatic wave was derived in [6] and the modulational instability was also investigated in the same paper. In [23], the classic Stokes expansion for periodic waves was extended to this physical setting and the resultant analytical solutions were compared with the numerical solutions to the fully nonlinear equations.

In the present paper, we extend the work of [22] by computing, using the time-dependent conformal mapping technique, solitary waves and their collision dynamics. In addition, the modulational instabilities in the

resonant cases are numerically examined in a similar manner to [24] which is concerned with the problem of flexural-gravity waves. The rest of the paper is structured as follows. The formulation and numerical scheme are introduced in sections 2 and 3, respectively. The results are presented and discussed in section 4. And finally, a conclusion is given in section 5.

2. Formulation

We consider an incompressible and inviscid fluid with density ρ of finite depth h bounded below by a flat rigid bottom. We introduce a two-dimensional Cartesian coordinate system with the x-axis along the undisturbed free surface and the y-axis directed vertically opposite to gravity. The upper boundary is free to move and denoted by $y = \zeta(x,t)$. The effect of surface tension and vorticity are both included. The former is expressed by $-\sigma\kappa$ with κ being the curvature. We define the vorticity by

$$\Omega = v_x - u_y \tag{3}$$

where (u, v) is the velocity field in the fluid region and the subscripts denote partial derivatives. For simplicity, we assume Ω is a constant and non-dimensionalize the problem by choosing

$$\left[\frac{\sigma}{\rho g}\right]^{1/2}, \qquad \left[\frac{\sigma}{\rho g^3}\right]^{1/4}, \tag{4}$$

as the reference length and time scale. In particular, the dimensionless fluid depth and vorticity are defined respectively by

$$h = \tilde{h}\left[\frac{\sigma}{\rho g}\right]^{1/2}, \quad \Omega = \tilde{\Omega}\Big/\left[\frac{\sigma}{\rho g^3}\right]^{1/4}. \tag{5}$$

The tildes in the non-dimensionalization are removed for the purpose of easy notations. The following system governs the motion of the fluid body and the deformation of the free surface

$$\phi_{xx} + \phi_{yy} = 0\,, \qquad \text{for } y < \zeta\,, \tag{6}$$

$$\phi_y = 0\,, \qquad \text{on } y = -h\,, \tag{7}$$

$$\zeta_t = \phi_y - \zeta_x\left(u_0 + \phi_x\right), \qquad \text{on } y = \zeta\,, \tag{8}$$

$$\phi_t + u_0\phi_x + \frac{1}{2}\left|\nabla\phi\right|^2 + \Omega\psi + \zeta - \kappa + B(t) = P_e\,, \qquad \text{on } y = \zeta\,. \tag{9}$$

Here ϕ is the potential function of the irrotational part, ψ is the harmonic conjugate of ϕ usually called the streamfunction, and $(u_0, v_0) = (U_0 - \Omega y, 0)$ is a trivial solution to the problem satisfying all the boundary

conditions where U_0 describes a constant speed at the undisturbed surface as shown in Figure 1. It is noted that we can always assume $U_0 = 0$ via introducing a moving frame of reference. In addition, the integral constant $B(t)$ can be absorbed by redefining the velocity potential ϕ, and P_e is the external forcing which is only considered in section 4.2 and zero otherwise.

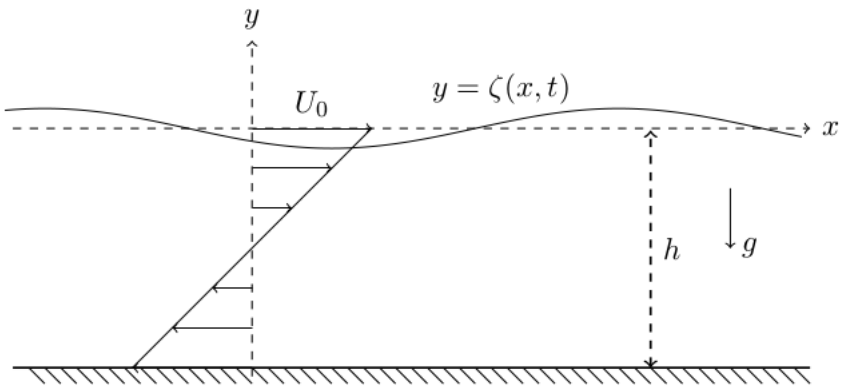

Figure 1. Schematic description of the physical problem.

2.1. Linear theory

By linearizing (6)–(9), the linear dispersion relation reads

$$kc_p^2 - \Omega c_p \tanh kh - (1 + k^2) \tanh kh = 0\,, \tag{10}$$

where k is the wavenumber and c_p is the phase speed. It has two distinct real solutions

$$c_p^{\pm} = \frac{\Omega \tanh kh \pm \sqrt{\Omega^2 \tanh^2 kh + 4k(1 + k^2) \tanh kh}}{2k}\,, \tag{11}$$

in which the wavenumber k is always kept positive and c_p^+ (c_p^-) is positive (negative) representing a right-moving (left-moving) wave. We denote by c_g ($= \omega_k$) the group velocity, where the frequency ω is a function of the wavenumber. The long-wave speed can be obtained from (11) by letting $k \to 0$, which takes the form of

$$c_0^{\pm} = \frac{\Omega h \pm \sqrt{\Omega^2 h^2 + 4h}}{2}\,. \tag{12}$$

For right-going waves, an elementary analysis of the derivative of c_p^+ yields

$$\begin{cases} c_p^+ \text{ is monotonically increasing in } k \text{ when } \mathcal{B} > \dfrac{1+\Omega c_0^+}{3}, \\ c_p^+ \text{ has a minimum } c_{\min} \text{ at } k = k_c\,(\neq 0) \text{ when } \mathcal{B} < \dfrac{1+\Omega c_0^+}{3}\,, \end{cases} \tag{13}$$

where the Bond number is defined as $\mathcal{B} = 1/h^2$ in dimensionless variables. Similarly, the version for left-moving waves can be obtained by letting $\Omega \to -\Omega$ and $c_0^+ \to c_0^-$. The former case in (13) is subsequently referred to the shallow-water regime or simply the shallow regime, whereas the latter is called the deep-water regime or the deep regime. We list some key facts for the deep regime as follows

1. the group speed reaches its minimum at $k = k_d$, and $k_d < k_c$;
2. the second harmonic resonance defined by $2\omega(k_s) = \omega(2k_s)$ occurs at $k = k_s$, and $k_s < k_c < 2k_s$;
3. the long-wave/short-wave interaction occurs at $k = k_l$, and $k_c < k_l$.

An illustrative graph is shown in Figure 2. It is noted that these comments stay valid for other problems with the same structure of the dispersion relation, e.g. flexural-gravity waves.

It is also noted that the criteria for the critical case $\mathcal{B}_c = (1+\Omega c_0)/3$ is in fact an equation for h whose value can be found numerically by an iterative scheme. It is discovered that $\mathcal{B}_c = 0.0544$ for $\Omega = -1$ and $\mathcal{B}_c = 0.8949$ for $\Omega = 1$. As summarized in Table 1, a left-moving wave and a right-moving wave can be in different regimes provided $\mathcal{B}$ is in a certain range. It is of great interest to study such break of symmetry of the curves for positive and negative phase speed, which does not take place in the irrotational case.

$\Omega = 1$	$0 < \mathcal{B} < 0.0544$	$0.0544 < \mathcal{B} < 0.8949$	$0.8949 < \mathcal{B}$
right-moving waves	deep	deep	shallow
left-moving waves	deep	shallow	shallow

Table 1
The type of linear regime for right-moving waves and left-moving waves when $\Omega = 1$.

To this end, we fix $h = 2.5$ and usually select $\Omega = \pm 1$ in the rest of the paper such that the associated Bond number is equal to 0.16 which lies in the interval $[\,0.0544\,, 0.8949\,]$. The two solutions to the quadratic equation (10) are depicted in Figure 3 for $\Omega = \pm 1$ and also $\Omega = 0$ for reference. We note that the dispersion relation (10) is invariant under the reflective transformation $(c_p, \Omega) \to (-c_p, -\Omega)$. Therefore we may choose $c_p > 0$

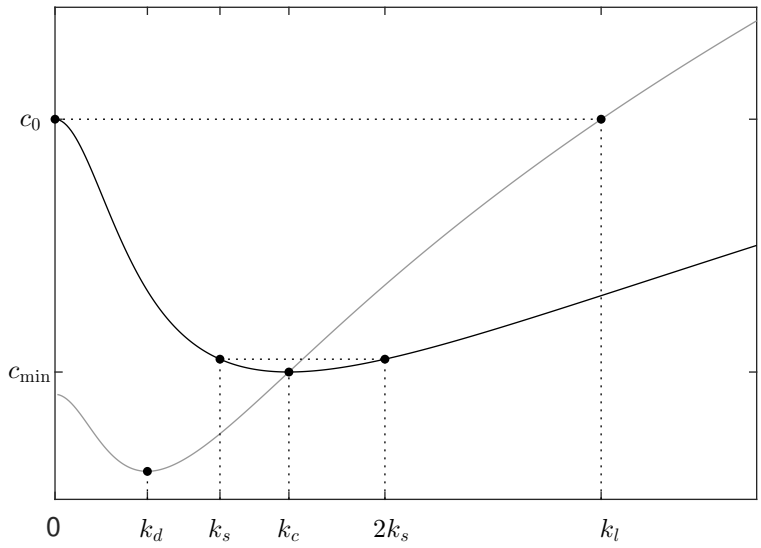

Figure 2. The curve of the phase speed $c_p(k)$ (in black) and the group speed $c_g(k)$ (in gray) in the so-called deep regime as defined in (13) .

(so all the superscripts $\pm$ are now dropped) and vary Ω to be positive or negative for studying unidirectional waves. In the irrotational case, the value of $\mathcal{B}$ equals 0.16 which is less than the critical value 1/3, i.e. in the deep-water regime. The theory predicts a phase speed minimum at a non-zero wavenumber marked with a diamond where wavepacket solitary waves may bifurcate. Since the phase speeds at $k = 0$ and $k \approx 2.0003$ are almost equal, the long wave can resonate with a Stokes wave so that elevation solitary waves with non-decaying oscillations in the far field, the so-called generalised solitary waves, are expected. In the presence of a positive vorticity $\Omega = 1$, the dispersion relation remains in the deep-water regime but the long wave resonates with a periodic wave with much larger wavenumber ($k \approx 10.25$). When $\Omega = -1$, the problem is in the shallow regime, i.e. c_p is always monotonically increasing in k. Depression solitary waves are expected to bifurcate at $k = 0$.

2.2. Nonlinear Schrödinger Equation

The nonlinear Schrödinger equation

$$\mathrm{i}\, A_\tau + \lambda A_{XX} + \gamma |A|^2 A = 0\,, \tag{14}$$

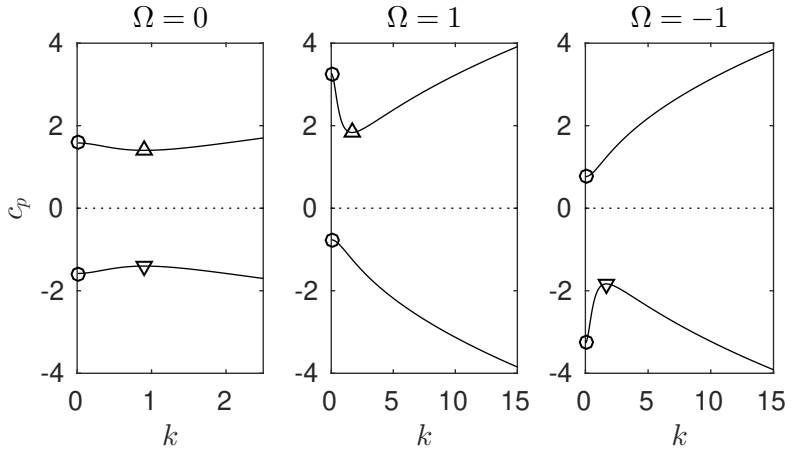

Figure 3. Graphs of the dispersion relation for $h = 2.5$ when $\Omega = 0$ (left), $\Omega = 1$ (middle) and $\Omega = -1$ (right). $k = 0$ are highlighted by circles. Phase speed minima are marked by triangles.

was derived in multi-scale variables $X = \epsilon x$, $\tau = \epsilon^2 t$, where ϵ is a small parameter, by [6] for capillary-gravity waves propagating on a linear shear current. Explicit expressions for λ and γ are given by equations (2.28) and (2.31) in [6], respectively, and the dimensionless version can be obtained by simply setting $\rho = 1$, $g = 1$ and $\sigma = 1$. The graphs of λ and γ from equation (14) against k in the deep regime are presented in figure 4. The results are qualitatively similar for different Ω, provided the deep-water regime criterion is met, with only a matter of scale. There is a zero for λ $(= \omega_{kk}/2)$ at $k = k_d$ where the group speed c_g $(= \omega_k)$ attains its minimum. Also, γ reaches zero at two positions $k = k_a$ & $k = k_b$ as marked in the bottom graph of figure 4. When $k \in \{k_a, k_b, k_d\}$, the cubic NLS is no longer valid as one of the coefficients becomes zero, and an equation with higher order dispersion or nonlinearity can be expected. Meanwhile, there are two asymptotes in the graph of γ corresponding to the second harmonic resonance at $k = k_s$ and long-wave/short-wave interaction at $k = k_l$, respectively. The weakly nonlinear theory breaks down at these two resonant points. To deal with such singularities, a different scaling is required to balance nonlinearity and dispersion, which will be further explored in sections 2.3 and 2.4.

As shown in [10], the existence of small-amplitude wavepacket solitary waves requires two conditions: (1) in the deep-water regime (2) the NLS at $k = k_c$ is of focussing type (i.e. $\lambda\gamma > 0$). As discussed in the last paragraph, the NLS swaps type at five specific wavenumbers k_a, k_b, k_d, k_s

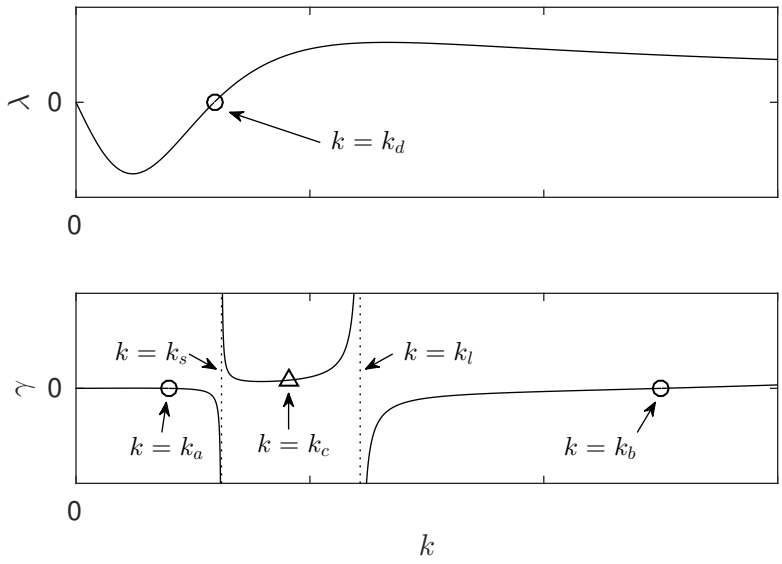

Figure 4. Graphs of the NLS coefficients in the deep-water regime versus the wavenumber k. This particular example is for $h = 2.5$ and $\Omega = 0$ with $k_a = 0.392$, $k_d = 0.592$, $k_s = 0.622$, $k_c = 0.907$, $k_l = 1.215$ and $k_b = 2.503$. The graphs are qualitatively similar for different h and Ω.

and k_l that are in fact the boundaries between the white and gray regions in the kh–$\mathcal{B}$ diagram shown in Figure 5 for $\Omega = \pm 1$. Also, we rediscover the fact that the NLS swaps type at $kh \simeq 1.363$ in the irrotational case ([25]), and we omit the detail here. In the presence of constant vorticity, the NLS is of focussing type in the limit $\mathcal{B} \to 0$ and $k \to 0$ ([26]). As the inequalities $k_d < k_c$ and $k_a < k_s < k_c < k_l$ are guaranteed, it can be readily shown that the NLS at $k = k_c$ (in the deep regime) stays always focussing regardless of the value of Ω or $\mathcal{B}$. Two examples for $\Omega = \pm 1$ from Figure 5 confirm the prediction as the black thick curves lie in white regions. The full diagram demonstrating the nature of the linear theory and the type of the weakly nonlinear regime for various Bond number (or simply the depth in the current scaling) and vorticity is displayed in Figure 6.

A general theory was developed by [4] regarding the modulational instability of periodic waves. It was shown that such instability occurs when the associated NLS is of focussing type. The problem was investigated by [6] for capillary-gravity waves on water of finite depth in the presence of a linear shear current in the non-resonant case. The modulational in-

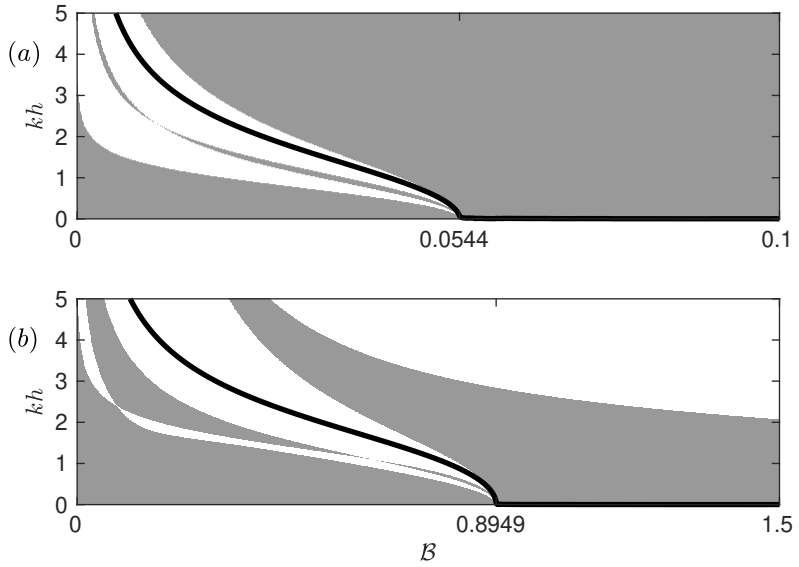

Figure 5. Graphs showing the type of NLS for different $\mathcal{B}$ and $\mu = kh$ when (a) $\Omega = -1$ and (b) $\Omega = 1$. White (gray) regions correspond to NLS focussing (defocussing) regime. The black thick curves represent the critical case $\mu = \mu_c$ where the phase speed attains its minimum. If $\mu_c = 0$, it is in the shallow regime. If $\mu_c > 0$, it is in the deep regime.

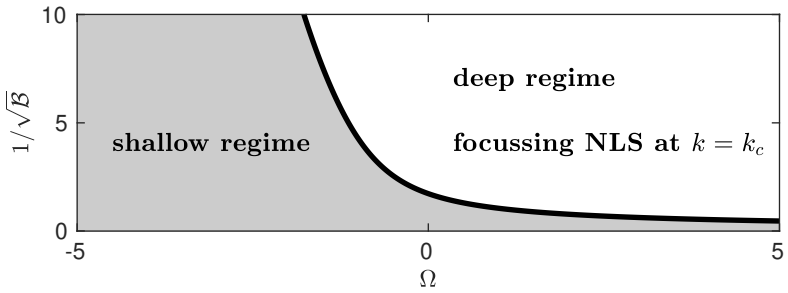

Figure 6. The gray region corresponds to the shallow regime where c_p is monotonically increasing. The white region is for the deep regime in which the associated NLS is always focussing at $k = k_c$. The black thick curve is the critical case $\mathcal{B} = (1 + \Omega c_0)/3$.

stabilities in the resonant cases are to be discussed by weakly nonlinear theories in sections 2.3 & 2.4, and numerically examined by fully nonlinear computations in section 4.3.

2.3. Second harmonic resonance

As previously introduced in Figure 2, there is a specific wavenumber k_s such that the associated propagating speed is identical to the speed of its second harmonic, i.e. $c_p(k_s) = c_p(2k_s)$ or equivalently

$$\omega^2(k_s)\tanh(k_s h) = 3k_s^3\,. \tag{15}$$

The equality (15) causes the coefficient of the nonlinear term in the NLS being singular. Under such circumstance, a modified multi-scale analysis with the inclusion of the second harmonic mode is needed. The unknown free surface η and the potential ϕ are functions of (X, T, τ) where

$$X = \epsilon x\,, \quad T = \epsilon t\,, \quad \tau = \epsilon^2 t\,. \tag{16}$$

Following [20], η can therefore be expanded about $y = 0$ as

$$\begin{aligned}\eta = {} & \epsilon\, A_{11}E + \epsilon\, A_{12}E^2 + \epsilon^2\, A_{21}E + \epsilon^2\, A_{22}E^2 + \epsilon^2\, A_{23}E^3 + \epsilon^2\, A_{24}E^4 \\ & + \epsilon^3\, A_{31}E + \epsilon^3\, A_{32}E^2 + \epsilon^3\, A_{33}E^3 + \epsilon^3\, A_{34}E^4 ... + \text{c.c.}\,,\end{aligned} \tag{17}$$

where $E = \exp(\mathrm{i}(kx - \omega t))$ and 'c.c.' stands for complex conjugate. The expansion of the potential function ϕ about $y = 0$ is obtained by solving the Laplace equation with the impermeability boundary condition (7). The detailed expression can be found in [19, 20]. Substituting the ansatz of η and ϕ into the kinematic condition (8) and the dynamic condition (9) on the free surface and collecting the coefficients of $\epsilon\, E$ and $\epsilon\, E^2$ at the leading order yields two solvability conditions

$$\omega(k)^2\coth(kh) - \Omega\omega(k) = k + k^3\,, \tag{18}$$

$$2\omega(k)^2\coth(2kh) - \Omega\omega(k) = k + 4k^3\,, \tag{19}$$

for non-trivial solutions for A_{11} and A_{12}, respectively. Combining (18) and (19) gives the criterion of the second harmonic resonance (15). By collecting the coefficients of $\epsilon^2\, E$ and $\epsilon^2\, E^2$ at the quadratic order yields the solvability conditions for A_{21} and A_{22}

$$A_{11_T} + c_g^{(1)} A_{11_X} = -ikc_1 A_{12} A_{11}^*\,, \tag{20}$$

$$A_{12_T} + c_g^{(2)} A_{12_X} = -ikc_2 A_{11}^2\,, \tag{21}$$

where

$$c_g^{(1)} = \omega_k(k)\,, \quad c_g^{(2)} = \omega_k(2k), \tag{22}$$

$$c_1 = \frac{\Omega^2 + \big[3\coth^2(kh) - 1\big]\omega^2 - \big[3\coth(kh) + \tanh(kh)\big]\Omega\omega}{2\omega\coth(kh) - \Omega}\,, \tag{23}$$

$$c_2 = \frac{\Omega^2 + \big[3\coth^2(kh) - 1\big]\omega^2 - \big[3\coth(kh) + \tanh(kh)\big]\Omega\omega}{4\omega\coth(2kh) - \Omega}\,. \tag{24}$$

The coefficient $c_g^{(1)}$ and $c_g^{(2)}$ are in fact the group speed for the first and second harmonic, respectively. It is also noted that quadratic equations (20)–(24) for the second harmonic resonance have the same form as those presented in [24] for flexural-gravity waves where the surface tension term is replaced by the flexural rigidity of plate. At the cubic order, collecting the coefficients of $\epsilon^3\,E$ and $\epsilon^3\,E^2$ from the kinematic and dynamic boundary conditions yields the solvability conditions for A_{31} and A_{32}

$$\begin{aligned}\mathrm{i}\,A_{11_\tau} + i\Big(A_{21_T} + c_g^{(1)}A_{21_X}\Big) + \lambda_1 A_{11_{XX}} + \mu_1|A_{11}|^2A_{11} + \mu_2|A_{12}|^2A_{11}\\ + \mu_3 A_{12}A_{21}^* + i\mu_4 A_{12}A_{11_X}^* + \mu_5 A_{22}A_{11}^* + i\mu_6 A_{12_X}A_{11}^* = 0\,,\end{aligned} \tag{25}$$

$$\begin{aligned}\mathrm{i}\,A_{12_\tau} + i\Big(A_{22_T} + c_g^{(2)}A_{22_X}\Big) + \lambda_2 A_{12_{XX}} + \nu_1|A_{11}|^2A_{12} + \nu_2|A_{12}|^2A_{12}\\ + \nu_3 A_{11}A_{21} + i\nu_4 A_{11}A_{11_X} = 0\,,\end{aligned} \tag{26}$$

with

$$\lambda_1 = \frac{\omega_{kk}(k)}{2}\,, \quad \lambda_2 = \frac{\omega_{kk}(2k)}{2}\,. \tag{27}$$

The terms in A_{23} and A_{24} have been eliminated by making use of the equalities derived from the terms in $\epsilon^2\,E^3$ and $\epsilon^2\,E^4$. Equations (25) and (26) are usually regarded as the counterparts to the standard cubic NLS on the occasion of the resonance. The coefficients of the nonlinear terms are extremely tedious, and hence we only present their values graphically as functions of Ω for a fixed h ($h = 2.5$ say) in Figure 7. There is a special value of Ω, denoted by Ω^* (which is found to be -0.475 in the case of $h = 2.5$), such that the wavenumber $k_s \to 0$. It is in fact the moment when the linear theory changes from the deep regime to the shallow regime. As shown in the bottom graph of Figure 7, μ_2, ν_1 and ν_2 become singular in the critical case $\Omega = \Omega^*$ causing a breakdown of the weakly nonlinear theory. It follows that the coupled system (25)–(26) stays valid only when $\Omega > \Omega^*$.

Combining (25)–(26) with (20)–(21) yields a system of four differential equations in $(A_{11}, A_{12}, A_{21}, A_{22})$ whose solutions were derived and

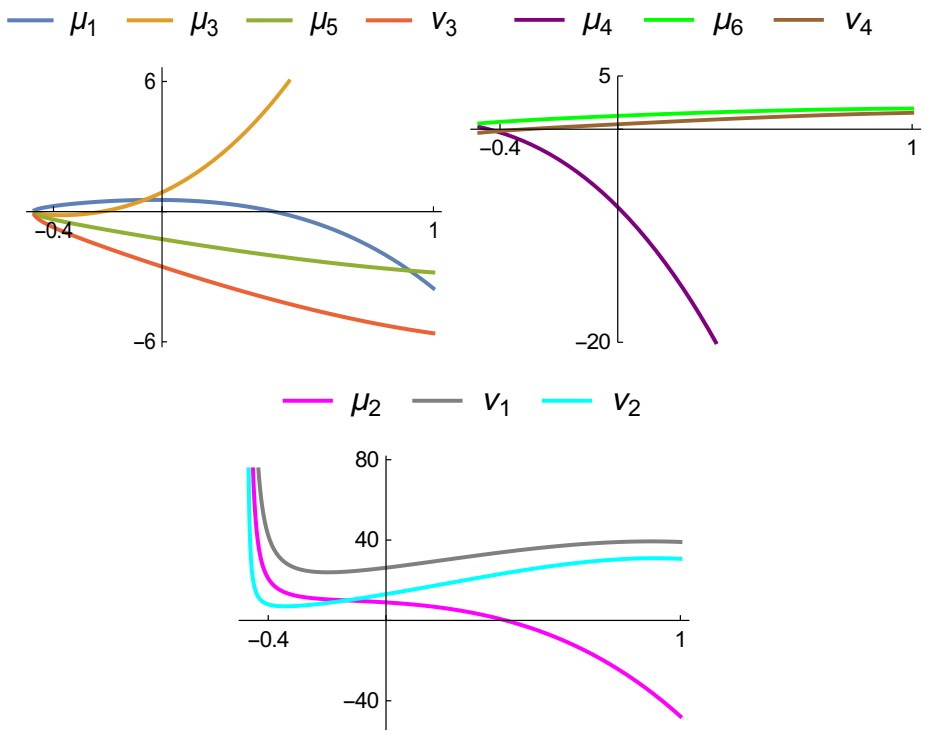

Figure 7. The graphs of the coefficients from Equation (25)-(26) versus the vorticity Ω when $h = 2.5$.

presented in [20]. The stability analysis can then be achieved by considering small perturbations in both first and second harmonics. Here we omit the detail since the approach is quite standard (the interested readers are refer to [20]). The instability was shown to be inevitable and occur at a sufficiently small modulational wavenumber for a given wave solution. This is similar to the Benjamin-Feir instability theory for a single carrier wave.

2.4. Long-wave/short-wave interaction

As illustrated in Figure 4, there is a singularity in the coefficient γ of the cubic NLS equation (2) since

$$c_g(c_g - \Omega h) = h \tag{28}$$

is satisfied at $k = k_l$ where the group speed c_g of the envelope matches the long wave speed c_0 from (12). Such phenomenon occurs among long waves and short waves on water of finite depth, and is usually addressed

as long-wave/short-wave interactions [27]. An alternative model equation is required as the associated cubic NLS becomes invalid. Following [5, 24], a new scaling is introduced as

$$X = \epsilon^{\frac{2}{3}}(x - c_g t)\,, \quad \tau = \epsilon^{\frac{4}{3}} t\,. \tag{29}$$

The surface elevation $\eta(X,\tau)$ and the potential function $\phi(X,y,\tau)$ are then expanded about $y = 0$ in the form of

$$\eta = \epsilon A e^{\mathrm{i}(kx-\omega t)} + \epsilon^{4/3}\eta_2 + \epsilon^{5/3}\eta_3 + \epsilon^2\eta_4 + \epsilon^{7/3}\eta_5 + \epsilon^{8/3}\eta_6 + \ldots \tag{30}$$

$$\phi = \epsilon^{2/3}\phi_0 + \epsilon\phi_1 + \epsilon^{4/3}\phi_2 + \epsilon^{5/3}\phi_3 + \epsilon^2\phi_4 + \epsilon^{7/3}\phi_5 + \ldots\,. \tag{31}$$

The detailed expansions are omitted here as the reader can be referred to [5, 24] for a review. The solvability condition arising from $O(\epsilon^{7/3})$ and the kinematic boundary condition at $O(\epsilon^{8/3})$ yield the evolution equations linking the short-wave envelope A and the long-wave velocity potential ϕ_0 as follows

$$\mathrm{i}\,A_\tau + \lambda A_{XX} = AB\,, \tag{32}$$

$$B_\tau = -\Delta\big(|A|^2\big)_X\,, \tag{33}$$

where $B = \delta\phi_{0X}$, $\lambda = \omega_{kk}/2$,

$$\Delta = \delta\Big[\frac{c_g\omega^2 + \omega\sinh(2kh)}{(2c_g - \Omega h)\sinh^2(kh)} - \frac{\Omega}{2c_g - \Omega h}\Big]\,, \tag{34}$$

$$\delta = k\left[1 + \frac{c_g - \Omega h}{2\omega\coth(kh) - \Omega}\Big(\omega^2\,\mathrm{csch}^2(kh) - 2\Omega\omega\coth(kh) + \Omega^2\Big)\right]. \tag{35}$$

It is noted that Δ and δ are the same as those found in [24] where the surface tension is replaced by the flexural rigidity of plate. The modulational instability can be studied by using the evolution equations (32)–(33) as highlighted in [5, 24]. It is discovered that there exists a threshold wavelength such that the instability occurs when the wavelength of the perturbation is longer than the threshold, which is analogous to the Benjamin-Feir theory.

3. Numerical Scheme

To solve the fully nonlinear equations numerically, we employ the time-dependent conformal mapping technique pioneered by [16], which maps the fluid region onto a fixed geometry, e.g. a strip with depth D, in a new complex plane denoted by $\xi + \mathrm{i}\eta$. We present all the functions in the new variables whose harmonic conjugate can be obtained via the Cauchy-Riemann equations for analytic functions. In the transformed

plane, we write the surface variables as $X(\xi,t) \triangleq x(\xi,0,t)$, $Y(\xi,t) \triangleq y(\xi,0,t)$, $\Phi(\xi,t) \triangleq \phi(\xi,0,t)$, $\Psi(\xi,t) \triangleq \psi(\xi,0,t)$. The conformal map can be explicitly solved as solutions of the following boundary value problems

$$y_{\xi\xi} + y_{\eta\eta} = 0, \qquad \psi_{\xi\xi} + \psi_{\eta\eta} = 0, \qquad \text{for} \quad -D < \eta < 0, \tag{36}$$

$$y = Y(\xi,t), \qquad \psi = \Psi(\xi,t), \qquad \text{on} \quad \eta = 0, \tag{37}$$

$$y = -h, \qquad \psi = Q, \qquad \text{on} \quad \eta = -D, \tag{38}$$

where $Y(\xi,t) = \zeta(\xi,0,t)$. Here Q is an arbitrary constant, and we choose $Q = \langle\Psi\rangle$ with $\langle\cdot\rangle$ being the mean value in ξ defined as

$$\langle f\rangle = \frac{1}{L}\int_{-L/2}^{L/2} f(\xi,\eta)d\xi\,, \tag{39}$$

where $\left[-\frac{L}{2},\frac{L}{2}\right]$ is the computational domain, and L is usually chosen as the wavelength in the physical space. It can be shown that

$$D = h + \langle Y\rangle\,, \quad X_\xi = 1 - \mathcal{T}[Y_\xi]\,, \quad \Psi_\xi = \mathcal{T}[\Phi_\xi]\,, \tag{40}$$

where $\mathcal{T}[.]$ is a transform defined by

$$\mathcal{T}[f](\xi) = \frac{1}{2D}\mathrm{PV}\int f(\xi')\coth\left[\frac{\pi}{2D}(\xi'-\xi)\right]d\xi'\,, \tag{41}$$

with 'PV' denoting the Cauchy principal value of the integral. By performing calculations similar to those presented in [28], we end up with the following time-evolution equations describing the surface motion

$$\begin{cases} X_\xi = 1 - \mathcal{T}\left[Y_\xi\right]\,, \quad \Phi_\xi = -\mathcal{T}\left[\Psi_\xi\right]\,, \\ Y_t = Y_\xi\mathcal{T}\left[\frac{\Psi_\xi - \Omega Y Y_\xi}{J}\right] - X_\xi\left(\frac{\Psi_\xi - \Omega Y Y_\xi}{J}\right)\,, \\ \Phi_t = \frac{\Psi_\xi^2 - \Phi_\xi^2}{2J} - Y + \kappa - \Omega\left(\Psi - \frac{Y X_\xi \Phi_\xi}{J}\right) + \Phi_\xi\mathcal{T}\left[\frac{\Psi_\xi - \Omega Y Y_\xi}{J}\right] + P_e\,, \end{cases} \tag{42}$$

where $\kappa = (Y_{\xi\xi}X_\xi - X_{\xi\xi}Y_\xi)/J^{3/2}$ and $J = X_\xi^2 + Y_\xi^2$ is the Jacobian of the conformal map.

The system can be further simplified for travelling waves translating at a constant velocity c,

$$\Psi = cY + \frac{\Omega}{2}Y^2\,, \tag{43}$$

$$\frac{1}{2J}\Big(c + \Omega Y X_\xi + \Omega\mathcal{T}[YY_\xi]\Big)^2 - \frac{c^2}{2} + Y - \kappa = P_e\,. \tag{44}$$

In the present paper, solitary waves are approximated by long periodic waves, therefore the surface elevation, which is assumed to be symmetric with respect to the vertical axis, can be expressed as a truncated Fourier

series

$$Y(\xi) = \sum_{n=-N/2}^{N/2} a_n \exp\left(\frac{2\,\mathrm{i}\, n\pi\xi}{L}\right) + \text{c.c}, \tag{45}$$

where the coefficients a_n are unknowns. Without lose of generality, we can set $a_0 = 0$. The symmetric condition implies that $a_n = a_{-n}$ for all n. The $\mathcal{T}$-transform is computed numerically via the Fourier multiplier

$$\mathcal{T}[f] = \mathcal{F}^{-1}\Big[\,\mathrm{i}\coth(kD)\mathcal{F}[f]\Big]\,, \tag{46}$$

where $\mathcal{F}$ denotes the Fourier transform. To achieve a high computational accuracy, in most computations for the solitary waves we select $N = 2048$ and $L = 80\pi$, and stop the Newton iteration when the residual error is less than 10^{-11}. For time-dependent simulations, $dt = 2.5 \times 10^{-4}$ is chosen. This numerical scheme has been successfully used in the context of gravity waves [28] and flexural-gravity waves [29] on water of finite depth.

4. Results

4.1. Free solitary waves

For $\Omega = 1$ and $h = 2.5$, the phase speed features a minimum at k_c ($\neq 0$) where the underlying NLS is focussing predicting the existence of decaying wavepackets as illustrated in section 2.2. The amplitude-speed bifurcation diagram in the full Euler equations, together with the NLS prediction, is presented in the left of Figure 8. Two branches of solutions have been discovered, and the amplitude parameter is defined by

$$A = \frac{\max\zeta(x) - \min\zeta(x)}{2\ \mathrm{sgn}\big(\zeta(0)\big)}\,, \tag{47}$$

where the sign function is included to distinguish between depression and elevation waves. Based on the NLS theory (see [30] for example), to leading order, the wave amplitude reads

$$||\zeta||_\infty \approx (c_{\min} - c)^{1/2}\sqrt{\frac{8k_c}{\gamma}}\,, \tag{48}$$

which indicates that the NLS is valid only for a very narrow range of speed. The bifurcation of elevation solitary waves, predicted by the KdV equation in the long wave regime, is shown on the right figure. Unlike KdV solitons, these so-called generalised solitary waves have non-decaying oscillations in the far field due to the resonance between the Stokes wave and long wave that travel at the same speed ($\approx c_0$). Two typical wave

profiles are plotted on the right-hand side of Figure 8. Because of the positive vorticity, the dispersion curve (10) becomes very broad, and solving the resonant condition $c(k) = c_0$ yields $k \approx 10.25$ indicating that the long wave interacts with a very short Stokes wave with wavelength 0.613 in the linear regime, or the 410th Fourier mode in the carrier wave with wavelength 80π. The Fourier spectrum of solution (*iii*) near the bifurcation point is examined. It is observed that the Fourier coefficients for high modes are of very small size comparable to the residual error from Newton's method except around the 413th mode where a peak appears as can be seen from the left graph of Figure 9, which confirms the prediction by the linear theory. On the other hand, the Fourier coefficients of the resonant modes are less than 10^{-10}, which results in the non-decaying oscillations of the generalized solitary waves being too small for visualization. Also, it is worth remarking that, for a larger vorticity, the resonant mode can be beyond the range of the Fourier modes computed. Then a larger N is required to observe the resonance via spectrum. In summary, the obtained generalized solitary waves are almost embedded solitons in the presence of a large vorticity.

In addition to the numerical evidence discussed in the previous paragraph, we examine on the value of curvature at $x = L/2$ denoted by κ_0 by either fixing Ω, A and varying $\mathcal{B}$ or fixing $\mathcal{B}$, A and varying Ω. Similar to [18], separated n-shaped and u-shaped curves, which correspond to branches of solutions with a crest and a trough at the end of the computational domain respectively, are obtained. As can be seen in the top graph of Figure 10, the results in the presence of a constant vorticity are qualitatively similar to the irrotational case, where the increase of $\mathcal{B}$ does not lead solutions to embedded solitons. In the bottom graph of Figure 10, the curves approach the horizontal axis as Ω increases and can get infinitely close to zero for a large vorticity ($\Omega = 1$ say), which shows that the obtained solutions are not but extremely close to embedded solitons. In fact, in the linear theory the embedded elevation soliton is the limit of generalised solitary waves as the vorticity tends to infinity where no resonance takes place and the end-point curvature becomes zero. In practice, the elevation generalised solitary waves obtained in the case of $\Omega = 1$ are already very good approximations to embedded solitons as illustrated early on.

For a negative vorticity $\Omega = -1$, the phase speed c_p is always monotonically increasing in k, and therefore solitary waves bifurcate from infinitesimal long waves in the limit $k \to 0$. The KdV equation predicts that the amplitude of a solitary wave is proportional to its wave speed (e.g. see [17]). This is confirmed by the numerical results as shown in Figure 11. In particular, solution (*vii*) is a static depression solitary wave which does not feature an overhanging structure.

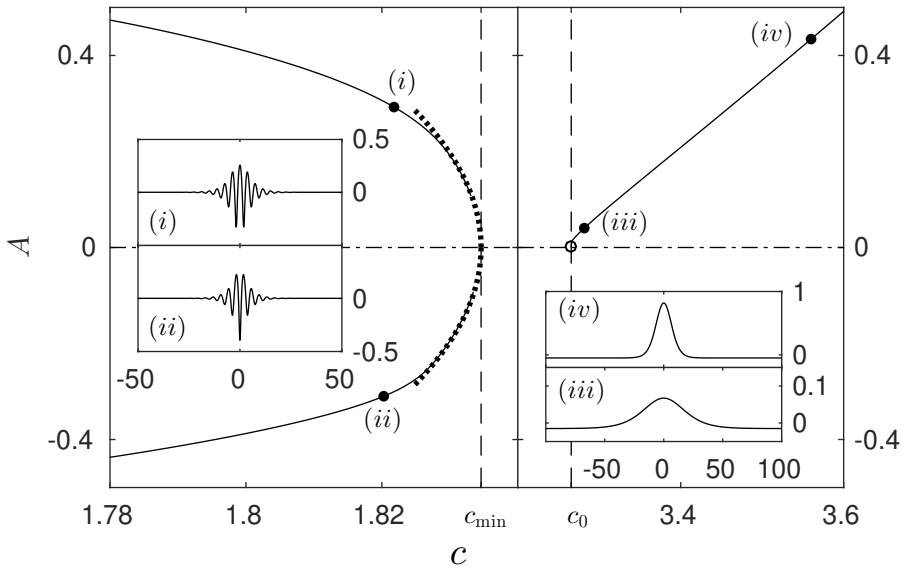

Figure 8. Bifurcation diagram of solitary waves for $\Omega = 1$ and $h = 2.5$. The long wave speed is $c_0 = 3.2656$, and the phase speed minimum is $c_{\min} = 1.8336$. Left: in the focussing NLS regime with the NLS prediction sketched in dotted curves. Wave profiles of (i) and (ii) are plotted in the physical plane. Right: in the long-wave regime. Wave profile (iii) and (iv) are plotted in the physical plane. Only part of the waves are shown for a better display.

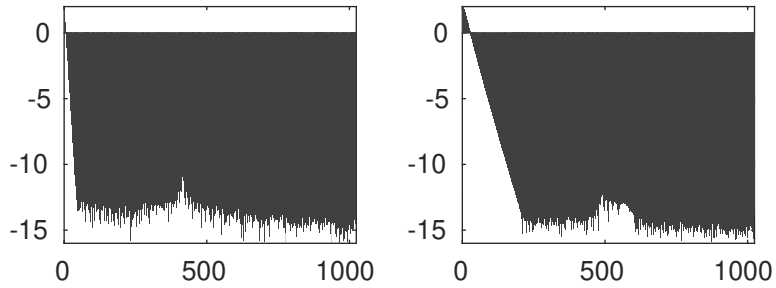

Figure 9. Left: the Fourier spectrum of solution (iii) from Figure 8 in the log-scale. Right: the Fourier spectrum of solution (iv) from Figure 8 in the log-scale.

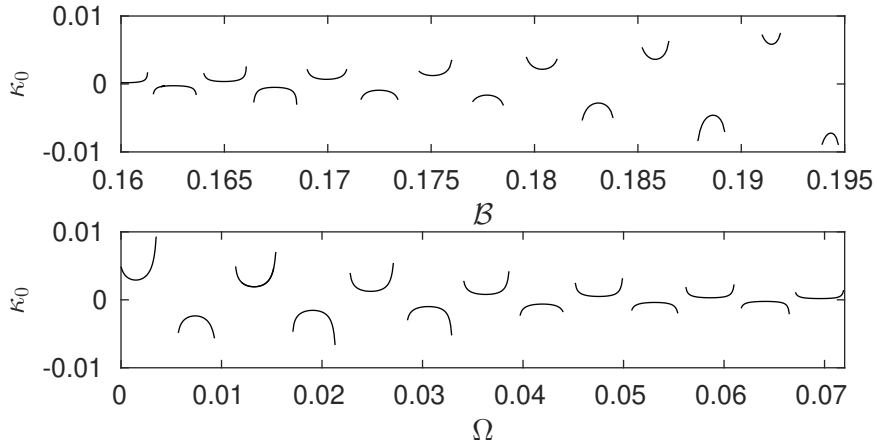

Figure 10. Top: the value of κ_0 versus $\mathcal{B}$ for elevation waves with $\Omega = 0.07$ and $A = 0.141$. Bottom: the value of κ_0 versus Ω for elevation waves with $A = 0.141$ and $\mathcal{B} = 0.16$.

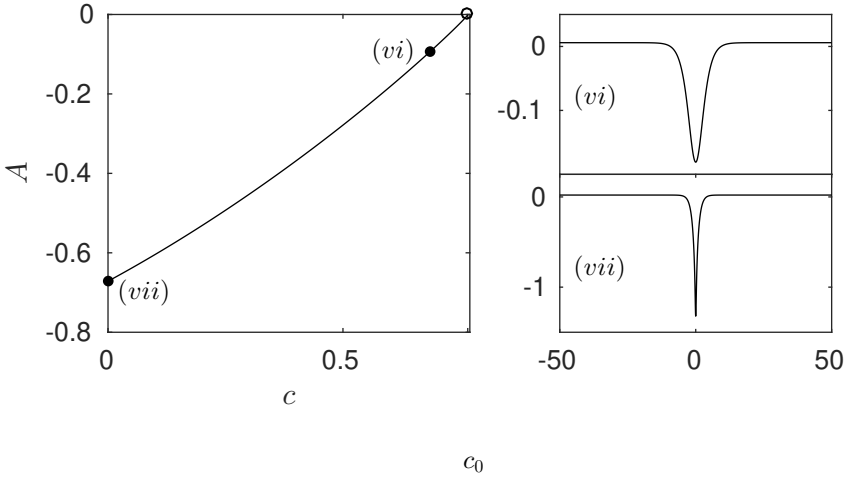

Figure 11. Bifurcation diagram of solitary waves in the long wave regime for $\Omega = -1$ and $h = 2.5$. The long wave speed c_0 is equal to 0.7656. Typical wave profiles are plotted in the physical x-y plane.

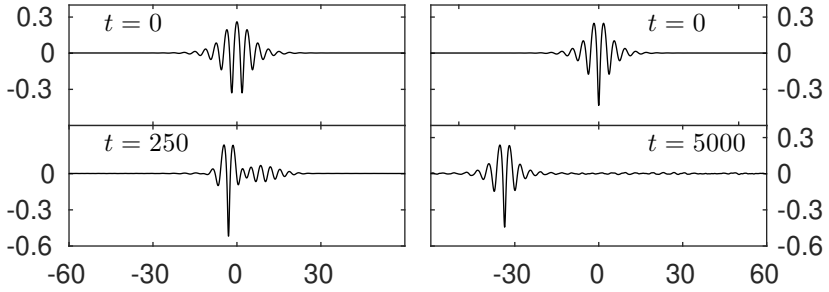

Figure 12. Left: dynamics of a wavepacket elevation solitary wave (*ii*) from Figure 8 with $c = 1.8218$ for $\Omega = 1$ and $h = 2.5$. A 1% perturbation in amplitude is imposed initially. Right: dynamics of a wavepacket depression solitary wave (*i*) from Figure 8 with $c = 1.8203$ for $\Omega = 1$ and $h = 2.5$. A 10% perturbation in amplitude is imposed initially. The snapshots only show part of the wave profiles. A frame of reference moving with the original wave speed is chosen in both experiments.

The longitudinal stability of the obtained solitary waves can be easily examined by the numerical algorithm given by [14, 29]. A small perturbation is superimposed initially on the exact solitary-wave solution. It is found from the left graph of Figure 12 that a wavepacket elevation wave is found to be unstable, and evolves in time to a wavepacket depression wave which is shown to be stable as can be seen in the right graph. The KdV-type solitary waves appear to be stable (see Figure 13).

Next, we perform the numerical computation of collision. The experiment is designed between two stable solitary waves moving in the opposite direction crossing each other. The most striking feature is that the system supports simultaneously counter-propagating stable solitary waves of different types, KdV-type and wavepacket solitary waves, since the underlying shear current modifies the Bond number differently for left- and right-propagating waves. As shown in Figure 14, both waves survive the interaction in the experiment, and small ripples can be observed after the interaction due to an inelastic nature of the collision.

4.2. Excitations of solitary waves

In this section, two numerical experiments of excitation of solitary waves are carried out, which are achieved by applying an external constant-moving forcing on the free surface. The experiments are simulated with $\Omega = 1$ by using the pressure distribution

$$P_e = A_0 e^{-(x - x_p - Ut)^2}, \tag{49}$$

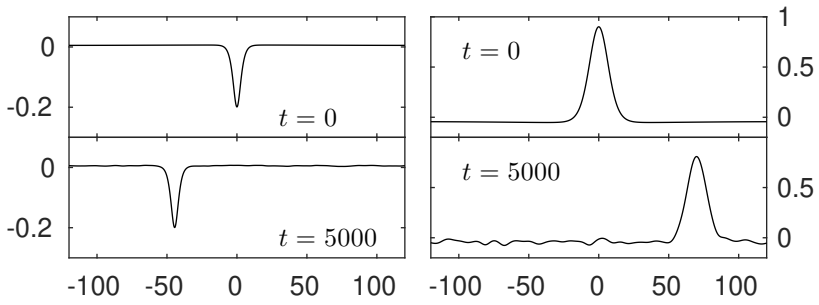

Figure 13. Left: dynamics of a KdV-type depression solitary wave (vi) from Figure 9 with $c = 0.6855$ for $\Omega = 1$ and $h = 2.5$. Right: dynamics of a generalized elevation solitary wave (iv) with $c = 3.56$ for $\Omega = 1$ and $h = 2.5$. A 10% perturbation in amplitude is imposed initially in both experiments. A frame of reference moving with the original wave speed is chosen.

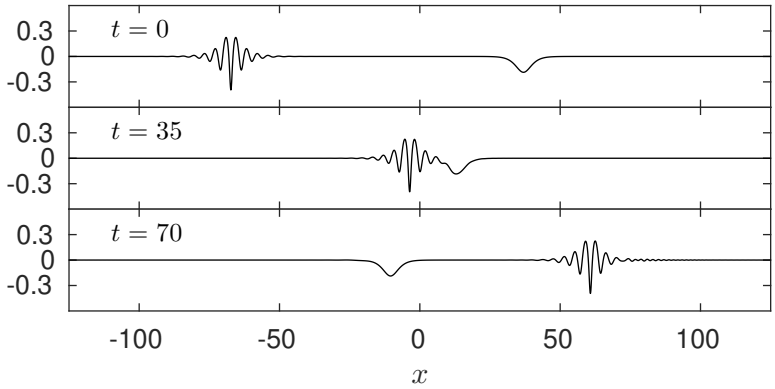

Figure 14. Head-on collision of a stable wavepacket solitary wave (i) moving rightwards with $c = 1.8203$ and a KdV-type depression solitary wave (vi) moving leftwards with $c = 0.6855$ in the presence of $\Omega = 1$.

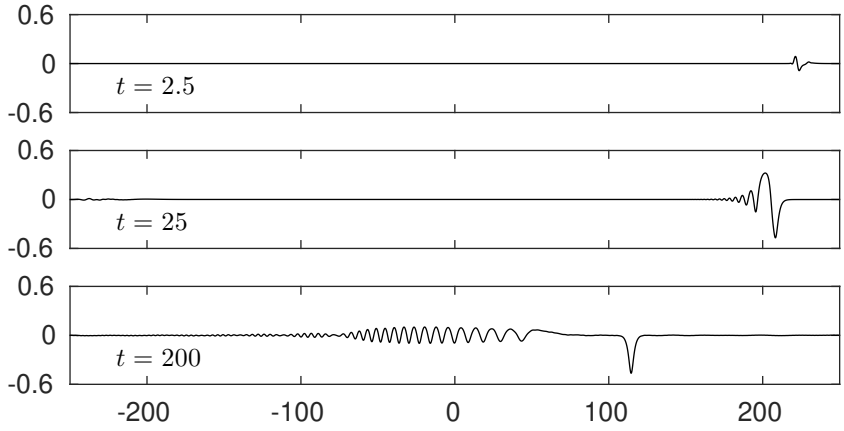

Figure 15. Excitation experiment 1. The external forcing is initially placed at $x = 225$ and travels leftwards with speed $U = 0.76$. It is switched on at $t = 0$ and off at $t = 25$.

where A_0 quantifies the strength of the forcing. The external forcing is launched at an initial position $x = x_p$ travelling rightwards with speed U (leftwards if U is negative) and removed after a sufficient period of time (at $t = t_s$). Both shallow and deep regimes are considered with appropriate values of the parameters.

1. To generate a KdV-type solitary wave, we choose $A_0 = 0.2$, $U = -0.76$, $x_p = -225$ and $t_s = 25$. As commented by [31], U is chosen to be close to the long wave speed where there is no travelling-wave solution with the forcing speed to the problem and the dynamic response to the external forcing is nonlinear. As can be seen from Figure 15, we observe the generation of a depression solitary wave as well as small ripples in front. If the forcing is kept active, then a very complex dynamics involving the periodic shedding of solitary waves can be expected (see e.g. [32]).

2. To excite a wavepacket solitary wave, we select $A_0 = 0.2$, $U = 2.1447$, $x_p = 225$ and $t_s = 25$. The value of U is chosen to be very close to the minimum of the phase speed where no steady responses exist in this transcritical regime. As presented in Figure 16, a stable depression wavepacket solitary wave is formed with the presence of noise ripples on the side. Similar to the excitation in the long-wave regime, if such forcing is always kept on, it can cause a periodic

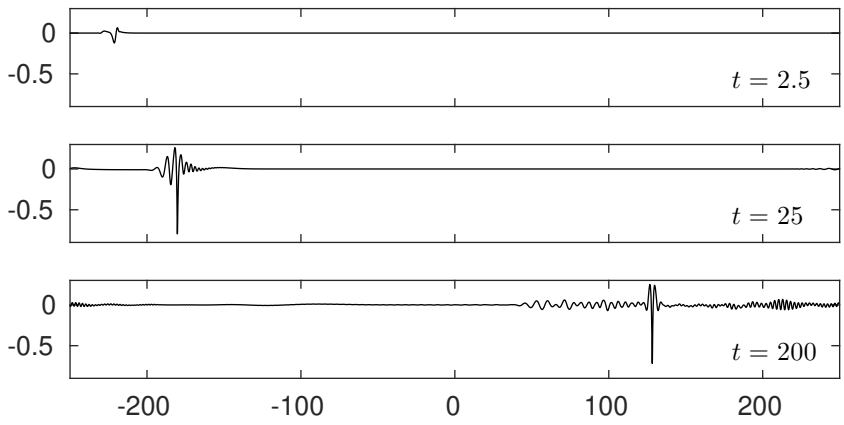

Figure 16. Excitation experiment 2. The external forcing is initially placed at $x = -225$ and travels leftwards with speed $U = 2.1447$. It is switched on at $t = 0$ and off at $t = 25$.

shedding of wavepacket solitary waves as numerically computed by [15] and experimentally observed by [33].

It is worth mentioning that the excitation of a depression solitary wave in the irrotational case is accompanied by a generalized elevation solitary wave in front as shown in [34] because of the small difference between the long wave speed ($c_0 = 1.51$) and the phase speed minimum ($c_{\min} = 1.403$). In the presence of vorticity, such difference becomes large (greater than 1.4 for $\Omega = 1$) so that the phenomenon of forming a generalized elevation solitary wave was not observed in the numerical experiment from Figure 16. Regarding the experiment shown in Figure 15, elevation solitary waves do not exist in the long wave regime. Therefore in both simulations (Figures 15 and 16), only small ripples have been observed accompanying the expected solitary waves at the end.

4.3. Modulational instability in resonant cases

The weakly nonlinear theories for the resonant cases from sections 2.3 and 2.4 predict the inevitable presence of the modulational instability provided that the modulational wavenumber is sufficiently small. In this subsection, the claims are to be examined numerically by the time-dependent computations for the full Euler equations. In the subsequent numerical experiments, an initial perturbation of magnitude α and modulational

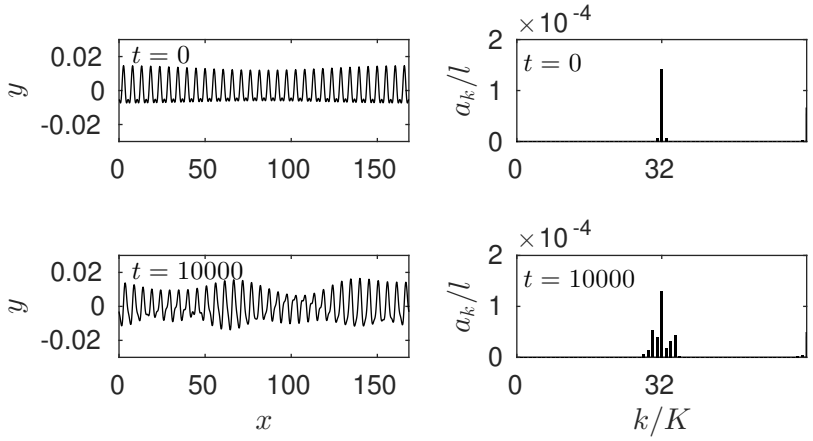

Figure 17. (Left) Time evolution of a Wilton solution with $k = k_s = 1.1946$, $h = 2.5$, $\Omega = 1$, $a = 0.01$, $c = 1.8993$, $l = 5.2597$, $L = 168.3109$ and $K = 0.0373$ which is initially given a modulational perturbation. The snapshots are taken at t = 0 and 10000. (Right) Fourier spectrum of the wave at $t = 0$ and 10000.

wavenumber K is imposed to the steady periodic solution ζ_0, namely

$$\zeta(x,0) = \Big[1 + \alpha\cos(Kx)\Big]\zeta_0(x)\,. \tag{50}$$

Regarding the second harmonic resonance, a Wilton solution with wavenumber k_s is selected for the computation with the following setting

- $\alpha = 0.1$, $K = k_s/32 = 0.0373$, $L = 32l = 168.3109$ with l being the wavelength of the carrier wave, $c = 1.8993$, $a = 0.01$.

In the case of the long-wave/short-wave resonance, a uniform wavetrain with $k = k_l$ is employed in the numerical experiment with the following parameters

- $\alpha = 0.1$, $K = k_l/64 = 0.0752$, $L = 64l = 83.5131$, $c = 2.3470$, $a = 0.01$.

From Figures (17) and (18), the modulational instabilities due to the generation and growth of the sideband Fourier modes have been clearly observed in both examples as expected. In addition, a strong long-wave component is generated in the case of the long-wave/short-wave interaction as can be seen from the Fourier spectrum in Figure 18.

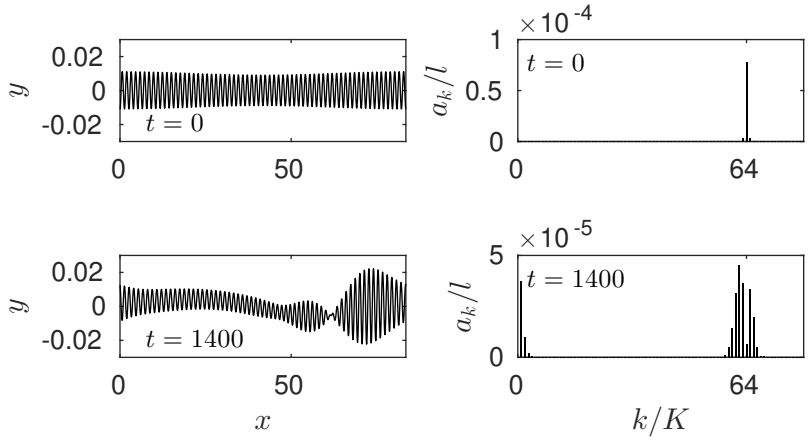

Figure 18. (Left) Time evolution of a uniform wavetrain with $k = k_l = 4.8151$, $h = 2.5$, $\Omega = 1$, $a = 0.01$, $c = 2.3470$, $l = 1.3049$, $L = 83.5131$ and $K = 0.0752$ which is initially given a modulational perturbation. The snapshots are taken at t = 0 and 10000. (Right) Fourier spectrum of the wave at $t = 0$ and 1400.

5. Conclusion

The problem of capillary-gravity waves on an incompressible and inviscid fluid of finite depth interacting with a linear shear current has been considered. The bifurcation and dynamics of solitary waves for different values of Ω were thoroughly investigated by a numerical method based on the time-dependent conformal mapping technique, and compared to the weakly nonlinear theory. When the phase speed features a global minimum, the interaction between long and shorts waves results in branches of generalized solitary waves. Though tails never vanish along these branches, for considerably large vorticity, almost embedded elevation solitary waves can be discovered. Time-dependent computations were achieved to examine the longitudinal instability of the obtained solutions. The vorticity modifies the Bond number differently for left- and right-propagating waves, and hence head-on collisions between solitary waves of different types are possible. A numerical experiment of the head-on collision was conducted between a KdV-type and a wavepacket type solitary waves, and inelastic behavior was observed though both solitary waves survive the collision. Simulations of solitary-wave excitation by a locally confined moving pressure disturbance were also performed. Meanwhile, the modulational instabilities for the resonant cases were investigated by the weakly nonlinear theories and fully nonlinear computations. To fur-

ther investigate the generation of wind ripples, a nonlinear shear profile is plausible (see [21] for example).

Acknowledgment

Z.W. was supported by the National Natural Science Foundation of China (no. 11772341) and the Strategic Priority Research Program of the Chinese Academy of Sciences (no. XDB22040203). P.A.M. was supported by the EPSRC grant (no. EP/N018176/1).

References

1. Zhang X. Capillary-gravity and capillary waves generated in a wind wave tank: observations and thoery. *J Fluid Mech.* 1995; 289:51–82.
2. Vanden-Broeck J-M. *Gravity-capillary free-surface flows.* Cambridge University Press; 2010.
3. Korteweg DJ & de Vries G. On the change of form of long waves advancing in a rectangular canal, and on a new type of long stationary waves. *Phil Mag J Sci.* 1895; 39:422–443.
4. Zakharov VE. Stability of periodic waves of finite amplitude on the surface of a deep fluid. *J Appl Mech Tech Phys.* 1968; 9:190–194.
5. Djordjevic VD & Redekopp LG. On two-dimensional packets of capillary-gravity waves. *J Fluid Mech.* 1977; 79:703–714.
6. Hsu H, Kharif C, Abid M & Chen Y. A nonlinear Schrödinger equation for gravity–capillary water waves on arbitrary depth with constant vorticity. Part 1. *J Fluid Mech.* 2018; 854:146–163.
7. Shabat A & Zakharov VE. Exact theory of two-dimensional self-focusing and one-dimensional self-modulation of waves in nonlinear media. *Sov Phys JETP.* 1972; 34:62.
8. Iooss G & Kirchgässner K. Bifurcation d'ondes solitaires en présence d'une faible tension superficielle. *C R Acad Sci Paris.* 1990; 311:265–268.
9. Iooss G & Kirrmann P. Capillary gravity waves on the free surface of an inviscid fluid of infinite depth. Existence of solitary waves. *Arch Rat Mech Anal.* 1996; 136:1–19.
10. Akylas TR. Envelope solitons with stationary crests. *Phys Fluids A.* 1993; 5:789–791.
11. Vanden-Broeck J-M & Dias F. Gravity-capillary solitary waves in water of infinite depth and related free-surface flows. *J Fluid Mech.* 1992; 240:549–557.
12. Yang TS & Akylas TR. On asymmetric gravity-capillary solitary waves. *J Fluid Mech.* 1997; 330:215–232.
13. Wang Z, Vanden-Broeck J-M & Milewski PA. Asymmetric gravity-capillary solitary waves on deep water. *J Fluid Mech.* 2014; 759:R2.
14. Milewski PA, Vanden-Broeck J-M & Wang Z. Dynamics of steep two-dimensional gravity-capillary solitary waves. *J Fluid Mech.* 2010; 664:466–477.
15. Wang Z. Stability and dynamics of two-dimensional fully nonlinear gravity-capillary solitary waves in deep water. *J Fluid Mech.* 2016; 809:530–552.

16. Dyachenko AI, Kuznetsov EA, Spector M & Zakharov VE. Analytical description of the free surface dynamics of an ideal fluid (canonical formalism and conformal mapping). *Phys Lett A.* 1996; 221:73–79.
17. Hunter JK & Vanden-Broeck J-M. Solitary and periodic gravity-capillary waves of finite amplitude. *J Fluid Mech.* 1983; 134:205–219.
18. Champneys AR, Vanden-Broeck J-M & Lord GJ. Do true elevation gravity–capillary solitary waves exist? A numerical investigation. *J Fluid Mech.* 2002; 454:403–417.
19. McGoldrick LF. On Wilton's ripples: a special case of resonant interactions. *J. Fluid Mech.* 1970; 42(1):193–200.
20. Jones MCW. Nonlinear stability of resonant capillary-gravity waves. *Wave Motion.* 1992; 15(3):267–283.
21. van Gastel K, Janssen PAEM & Komen GJ. On phase velocity and growth rate of wind-induced gravity-capillary waves. *J Fluid Mech.* 1985; 161:199–216.
22. Kang Y & Vanden-Broeck J-M. Gravity-capillary waves in the presence of constant vorticity. *Eur J Mech B/Fluids.* 2000; 19:253–268.
23. Hsu H, Francius M, Montalvo P & Kharif C. Gravity-capillary waves in finite depth on flows of constant vorticity. *Proc R Soc A.* 2016; 472:20160363.
24. Gao T, Wang Z & Milewski PA. Nonlinear hydroelastic waves on a linear shear current at finite depth. *J Fluid Mech.* 2019; 876:55–86.
25. Benjamin TB & Feir JE. The disintegration of wave trains on deep water Part 1. Theory. *J Fluid Mech.* 1967; 27(3):417–430.
26. Thomas R, Kharif C & Manna M. A nonlinear Schrödinger equation for water waves on finite depth with constant vorticity. *Phys Fluids.* 2012; 24(12):127102.
27. Benney DJ. A general theory for interactions between short and long waves. *Stud Appl Maths.* 1977; 56(1):81–94.
28. Choi W. Nonlinear surface waves interacting with a linear shear current. *Math Comput Simul.* 2009; **80**:29–36.
29. Gao T, Vanden-Broeck J-M & Wang Z. Numerical computations of two-dimensional flexural-gravity solitary waves on water of arbitrary depth. *IMA J Appl Math.* 2018; 83:436–450.
30. Wang Z & Milewski PA. Dynamics of gravity-capillary solitary waves in deep water. *J Fluid Mech.* 2012; 708:480–501.
31. Milewski PA, Vanden-Broeck J-M & Wang Z. Hydroelastic solitary waves in deep water. *J Fluid Mech.* 2011; 679:628–640.
32. Wu TYT. Generation of upstream advancing solitons by moving disturbances. *J Fluid Mech.* 1987; 184:75–99.
33. Diorio J, Cho Y, Duncan JH & Akylas TR. Gravity-capillary lumps generated by a moving pressure source. *Phys Rev Lett.* 2009; 103(21):214502.
34. Gao T, Doak A, Vanden-Broeck J-M & Wang Z. Capillary-gravity waves on a dielectric fluid of finite depth under normal electric field. *Eur J Mech B/Fluids.* 2019; 77:98–107.